The Astrophysical Journal, 898:62 (14pp), 2020 July 20 https://doi.org/10.3847/1538-4357/ab9951

Gravitational Potential and Surface Density Drive Stellar Populations. II. Star-forming Galaxies

Tania M. Barone[1,2,3], Francesco D'Eugenio[4], Matthew Colless[1,3], and Nicholas Scott[2,3]
[1] Research School of Astronomy and Astrophysics, The Australian National University, Canberra, ACT 2611, Australia; tania.barone@anu.edu.au
[2] Sydney Institute for Astronomy, School of Physics, The University of Sydney, NSW, 2006, Australia
[3] ARC Centre of Excellence for All Sky Astrophysics in 3 Dimensions (ASTRO 3D), Australia
[4] Sterrenkundig Observatorium, Universiteit Gent, Krijgslaan 281 S9, B-9000 Gent, Belgium
Received 2019 October 16; revised 2020 May 19; accepted 2020 May 31; published 2020 July 23

Abstract

Stellar population parameters correlate with a range of galaxy properties, but it is unclear which relations are causal and which are the result of another underlying trend. In this series, we quantitatively compare trends between stellar population properties and galaxy structural parameters in order to determine which relations are intrinsically tighter, and are therefore more likely to reflect a causal relation. Specifically, we focus on the galaxy structural parameters of mass M, gravitational potential $\Phi \sim M/R_e$, and surface mass density $\Sigma \sim M/R_e^2$. In Barone et al. we found that for early-type galaxies (ETGs) the age–Σ and [Z/H]–Φ relations show the least intrinsic scatter as well as the least residual trend with galaxy size. In this work we study the ages and metallicities measured from full spectral fitting of 2085 star-forming galaxies (SFGs) from the SDSS Legacy Survey, selected so all galaxies in the sample are probed to one effective radius. As with the trends found in ETGs, we find that in SFGs age correlates best with stellar surface mass density, and [Z/H] correlates best with gravitational potential. We discuss multiple mechanisms that could lead to these scaling relations. For the [Z/H]–Φ relation we conclude that gravitational potential is the primary regulator of metallicity, via its relation to the gas escape velocity. The age–Σ relation is consistent with compact galaxies forming earlier, as higher gas fractions in the early universe cause old galaxies to form more compactly during their in situ formation phase, and may be reinforced by compactness-related quenching mechanisms.

Unified Astronomy Thesaurus concepts: Scaling relations (2031); Galaxy stellar content (621); Galaxy ages (576); Galaxy abundances (574); Extragalactic astronomy (506)

Supporting material: machine-readable table

1. Introduction

The stellar population of a galaxy is a cumulative record of the history of the formation and assembly of its stars. Different stellar population parameters each provide a piece of this complex puzzle. Stellar population age is determined both by when the galaxy first formed stars and how long ago star formation was quenched. Total metallicity [Z/H] tells us about the number of generations of stars the galaxy has formed and whether the current population formed from pristine gas or recycled material. In a complementary fashion, α-enhancement [α/Fe] provides a measure of star formation duration, by indicating the extent to which the iron, produced in Type Ia supernovae by relatively long-lived stars, is recycled into subsequent stellar populations (e.g., Greggio & Renzini 1983; Worthey 1992; Matteucci 1994; Pagel & Tautvaisiene 1995; Thomas et al. 1998, 2005; McDermid et al. 2015). Using all three of these parameters, we can attempt to reconstruct the broad features of a galaxy's evolutionary history. Understanding what drives changes in these quantities provides insights into the processes shaping galaxy assembly and star formation.

Stellar population parameters have been found to correlate with a wide range of galaxy properties. Many studies have focused on the dependence of stellar population on mass (Gallazzi et al. 2005, 2006; Thomas et al. 2010; González Delgado et al. 2015; Lian et al. 2018) and velocity dispersion σ (early types: Nelan et al. 2005; Thomas et al. 2005; Robaina et al. 2012; late types: Ganda et al. 2007; early spirals: Peletier et al. 2007). Other works have investigated correlations with initial mass function (IMF; La Barbera et al. 2013), morphological type (Ganda et al. 2007; Scott et al. 2017), central black hole mass (Martín-Navarro et al. 2016), and structural lopsidedness (Reichard et al. 2009). However it is unclear which (if any) of these correlations imply causation and which are the result of other underlying trends—for example, until recently it was uncertain whether the population–environment relations are causal (Thomas et al. 2005; Sánchez-Blázquez et al. 2006a; Schawinski et al. 2007b) or the result of both stellar population and environment correlating with stellar mass M_* (Thomas et al. 2010; McDermid et al. 2015). Recent studies by Liu et al. (2016) and Scott et al. (2017) have reconciled this disparity, showing that dependence on mass alone is insufficient to explain observed trends and environment plays a measurable, albeit secondary, role. Furthermore, it is unclear whether the well-studied color–magnitude relation is a consequence of both parameters correlating with σ (Bernardi et al. 2005) or M_* (Gallazzi et al. 2006). The difficulty is that these trends are often not directly comparable, due to different observational and model uncertainties, and one correlation appearing stronger than another may simply reflect a higher precision in the measurements rather than underlying physics.

By quantitatively comparing scaling relations, several recent studies have demonstrated a clear effect of galaxy size R_e on stellar population for galaxies ranging from highly star forming to quiescent. Franx et al. (2008) found that for massive galaxies out to $z \sim 2$, M_* alone is not a good predictor of star formation

history and that color as a function of stellar mass surface density $\Sigma \propto M_*/R_e^2$ or gravitational potential $\Phi \propto M_*/R_e$ (referred to as "inferred velocity dispersion") shows less scatter than as a function of M_*. This was extended to low redshifts ($z < 0.11$) by Wake et al. (2012), who, by quantifying residual trends when one parameter is held fixed, asserted that $u - r$ color correlates more strongly with σ than Σ, Sérsic index (Sérsic 1968), or M_*. Using spectroscopically derived stellar population parameters for low redshift samples, Scott et al. (2017) and Li et al. (2018) showed that for both early- and late-type galaxies much of the scatter in population–mass relations is due to variations with galaxy size, by demonstrating how stellar population varies in the mass–size plane (see also McDermid et al. 2015 for early types). Additionally, van de Sande et al. (2018) showed stellar age is tightly coupled with intrinsic ellipticity for both early- and late-type galaxies.

In Barone et al. (2018, hereafter Paper I) we quantitatively compared global stellar population trends in morphologically identified early-type galaxies (ETGs) by analyzing both their intrinsic scatter and residual trends. We focused on the three structural parameters mass M, gravitational potential $\Phi \propto M/R_e$, and surface density $\Sigma \propto M/R_e^2$. For each structural parameter we employed two mass estimators: a dynamical mass based on spectroscopic velocity dispersion σ and the virial theorem ($M_D \propto \sigma^2 R_e$) and a stellar mass based on photometric luminosity and color (M_*). We showed that correlations with σ are reproduced using the purely photometric estimator of potential M_*/R_e. We found the tightest correlations, and the least residual trend with galaxy size, for the $g - i$ color–Φ, [Z/H]–Φ, and age–Σ relations. We found [α/Fe] to correlate strongly with both Σ and Φ. We concluded that: (1) the color–Φ diagram is a more precise tool for determining the developmental stage of a stellar population than the color–M diagram; and (2) Φ is the primary regulator for global stellar metallicity, via its relation to the gas escape velocity. The latter is supported by the results of D'Eugenio et al. (2018), who showed that gas-phase metallicity in star-forming galaxies (SFGs) is also more tightly correlated with Φ than either M or Σ. With regards to the age–Σ and [α/Fe]–Σ correlations, we proposed two possible explanations: either they are the result of compactness-driven quenching mechanisms or they are fossil records of the $\Sigma_{\rm SFR} \propto \Sigma_{\rm gas}$ relation in their disk-dominated progenitors (or some combination of these). To determine which of the various possible physical mechanisms are responsible, we need to know whether these scaling relations are also present in earlier phases of galaxy evolution while they are still forming stars.

In this paper (Paper II), we build on the results on stellar populations in ETGs presented in Paper I and on gas-phase metallicity in SFGs by D'Eugenio et al. (2018), by studying the ages and metallicities of SFG stellar populations and how they correlate with stellar mass (M_*), gravitational potential ($\Phi \propto M_*/R_e$) and surface mass density ($\Sigma \propto M_*/R_e^2$). The overarching approach of this series is to quantitatively compare trends between stellar properties and galaxy dynamics and structure, with the aim of finding the strongest/tightest scaling relations. This paper is arranged as follows. In Section 2 we detail the sample selection, and why the data set used has changed from Paper I. Section 3 describes the full spectral fitting method used to measure the stellar population ages and metallicities. In Section 4 we present our analysis methods and results for the luminosity-weighted parameters, and in Section 5 we present the mass-weighted results. In Section 6 we discuss our results and the possible mechanisms responsible, and qualitatively compare to the results presented in Paper I. Finally we provide a summary in Section 7. Although we perform both luminosity-weighted and mass-weighted fits, we focus predominantly on the luminosity-weighted parameters. Given the galaxies in our sample are star forming, their spectra are dominated by young stars and so the contribution from low-luminosity old stars is not well constrained, making it difficult to recover the true mass-weighted parameters. Throughout this paper we use the terms "early" and "late" type to refer to a visual morphological classification, whereas "quiescent" and "star forming" are based on measured star formation rates (SFRs). While early type and star forming are not mutually exclusive categories, we note that the overlap between them is small. Only 7% of early types in our sample from Paper I would also be classified as star forming. Therefore for our purposes the categories can be considered disjoint. We assume a Lambda cold dark matter (ΛCDM) cosmology with $\Omega_M = 0.3$, $\Omega_\Lambda = 0.7$, and $H_0 = 70$ km s^{-1} Mpc^{-1}, and a Chabrier (2003) IMF.

Table 1
Description of the Table Containing Our Derived Stellar Population Parameters along with the Stellar Masses from Kauffmann et al. (2003a) and Effective Radii from Simard et al. (2011)

Column Name	Units	Description
specObjID	⋯	SDSS spectroscopic object ID
ObjID	⋯	SDSS photometric object ID
Plate	⋯	SDSS plate ID
MJD	⋯	Modified Julian date of observation
FiberID	⋯	SDSS fiber ID
z	⋯	SDSS spectroscopic redshift
logAge-L	$\log_{10}$ Gyr	Luminosity-weighted age
e_logAge-L	$\log_{10}$ Gyr	Uncertainty on luminosity-weighted age
[Z/H]-L	⋯	Luminosity-weighted total metallicity
e_[Z/H]-L	⋯	Uncertainty on luminosity-weighted total metallicity
logAge-M	$\log_{10}$ Gyr	Mass-weighted age
e_logAge-M	$\log_{10}$ Gyr	Uncertainty on mass-weighted age
[Z/H]-M	⋯	Mass-weighted total metallicity
e_[Z/H]-M	⋯	Uncertainty on mass-weighted total metallicity
logM*	$\log_{10} M_\odot$	Stellar mass from Kauffmann et al. (2003a)
e_logM*	$\log_{10} M_\odot$	Uncertainty on stellar mass from Kauffmann et al. (2003a)
R_e	kpc	Circularized effective radius in r-band from Simard et al. (2011)

(This table is available in its entirety in machine-readable form.)

2. Sample Selection

All data used in this paper is publicly available and based on the SDSS Legacy Survey (York et al. 2000; Strauss et al. 2002). An electronic table of the catalog data as well as our derived stellar population parameters is available online, and is described in Table 1. For our stellar population measurements we use optical spectra from Data Release 7 (Abazajian et al. 2009). We use r-band effective radii (R_e) from Simard et al. (2011), as they provide both single and various double Sérsic fits as well as an F-test probability to determine the most appropriate model for each galaxy. To convert from apparent to physical size we use the spectroscopic redshifts given by the

SDSS pipeline and assume the standard ΛCDM cosmology. We use H_α-derived specific star formation rates (sSFRs; Brinchmann et al. 2004) from the MPA/JHU catalog, and select SFGs as having a total sSFR $>10^{-11.0}M_\odot yr^{-1}$, and "star-forming" locations on the BPT diagram (Baldwin et al. 1981; Veilleux & Osterbrock 1987; Kewley et al. 2001; Kauffmann et al. 2003a; Schawinski et al. 2007a) as defined by Thomas et al. (2013). To ensure reliable stellar population measurements, we select spectra with a median spectral signal-to-noise ratio (S/N) $\geqslant$15 per Å. We use stellar masses (M_*) from Kauffmann et al. (2003a) and Salim et al. (2007), which are derived from spectral energy distribution fitting. The M_* from Kauffmann et al. (2003a) are based on a Kroupa (2001) IMF, whereas the stellar population models use a Chabrier (2003) IMF. Hence, we rescale M_* to a Chabrier (2003) IMF using the conversion from Madau & Dickinson (2014), $\log M_{\rm Chabrier} = \log M_{\rm Kroupa} - 0.034$.

We compare M_* from Kauffmann et al. (2003a) with M_* derived from our full spectral fits, as well as the M_* derived by Chang et al. (2015) using SDSS spectra and photometry from the Wide-field Infrared Survey Explorer (Wright et al. 2010), and find good agreement between all three measurements. We prefer to use a partially independent measure of M_* rather than the values derived from our full spectral fits to reduce the correlated errors between M_* and the stellar population parameters. The stellar masses derived by Chang et al. (2015) use the radius measurements by Simard et al. (2011) that we also use in our fits, so to reduce the effect of correlated errors between M_* and R_e artificially tightening the trends, we use M_* from Kauffmann et al. (2003a). We note, however, that our results are quantitatively unchanged if we instead use the stellar masses from Chang et al. (2015) or from our full spectral fits.

In Paper I we used a different data set, namely 625 ETGs from the Sydney-AAO Multi-object Integral-field (SAMI) galaxy survey (Croom et al. 2012; Bryant et al. 2015; Scott et al. 2018). However, the comparatively extended ongoing star formation in SFGs leads to a higher intrinsic scatter in single-burst parameterizations, so here we require a larger sample than SAMI provides in order to determine the same scaling relations.

2.1. Aperture-matched Sampling (AMS)

We employ the AMS technique used by D'Eugenio et al. (2018), in which galaxies are selected to have similar physical areas encompassed by the fiber aperture. This technique allows us to mimic the adaptive aperture of integral-field surveys while taking advantage of the large and diverse data sets of single-fiber surveys such as the SDSS Legacy Survey. The AMS approach mitigates (at the expense of sample size) the aperture bias inherent to single-fiber surveys that results from probing galaxies over varying areas depending on their apparent size. Combined with radial trends within galaxies, aperture bias can lead to spurious global trends. The aperture-matched subsample is defined by $R_e = R_{\rm fiber}(1 \pm t)$ for some small tolerance t. Following D'Eugenio et al. (2018) we use a tolerance of 13%; given the SDSS Legacy Survey fiber radius of 1.5″, this criterion selects galaxies with $1.3'' < R_e < 1.7''$. Due to our aperture-matched criterion, our sample has a correlation between galaxy size and redshift. We therefore also require a sample with a narrow range in redshift to remove the effect of our results being due to evolution with redshift rather than dependence on size. We select galaxies with spectroscopic redshifts $0.043 < z < 0.073$.

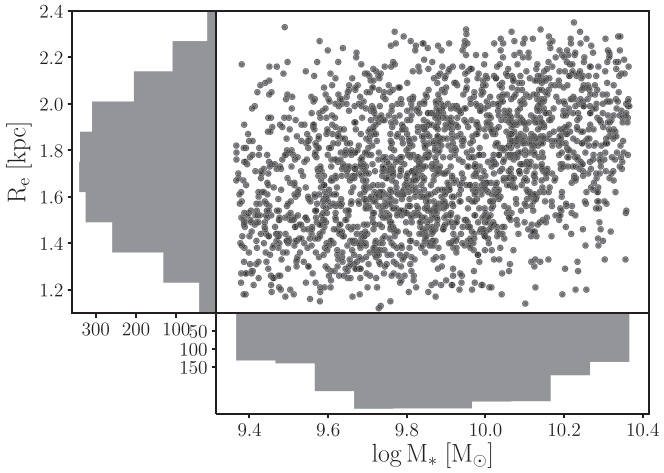

Figure 1. Mass–size plane for the sample of SDSS galaxies used here. The sample is approximately evenly distributed in R_e at fixed M_*, which reduces bias when determining the dependence of stellar population parameters on size.

2.2. Mass-limited Sample

In order to investigate the relative importance of mass and size in predicting stellar population parameters, it helps for the sample to have a similar size distribution at any fixed mass, so there is less in-built mass–size correlation (see Figure 1). Consequently we select a mass-limited sample defined by $9.434 < \log(M_*/M_\odot) < 10.434$. The final sample still has a residual mass–size dependence in that higher-mass galaxies have a larger mean size, as removing this completely would severely compromise sample size. While the distribution of sizes at the high- and low-mass ends of our sample are not identical, the change in the range of sizes is small; the mean size of the galaxies in the lowest and highest mass bins in Figure 1 (of width 0.1 dex) are 1.58 and 1.88 kpc, respectively.

3. Stellar Population Synthesis

We measure the stellar population parameters from full spectral fits using theoretical stellar population models based on the Medium resolution INT Library of Empirical Spectra (MILES; Sánchez-Blázquez et al. 2006b; Vazdekis et al. 2010, 2015), using a Bag of Stellar Tracks and Isochrones (BaSTI) isochrones (Pietrinferni et al. 2004, 2006) and a Chabrier (2003) IMF. This is different from the Lick index method and the models used in Paper I. The stellar population parameters for Paper I were measured by Scott et al. (2017) using the popular Lick system of absorption line indices and the models by Schiavon (2007) and Thomas et al. (2011), as Lick indices afford a benchmark for the analysis of ETG (and globular cluster) populations (Faber 1973). The little-to-no ongoing star formation in ETGs means the spectral absorption lines are free from emission by ionized interstellar gas, allowing for precise measurements. In contrast, SFGs have emission from ionized gas contaminating the absorption features, making it difficult to make accurate measurements. Nevertheless, with high S/N spectra and careful masking of emission lines, Ganda et al. (2007) and Peletier et al. (2007) were able to find scaling relations with mass and velocity dispersion similar to those found in ETGs.

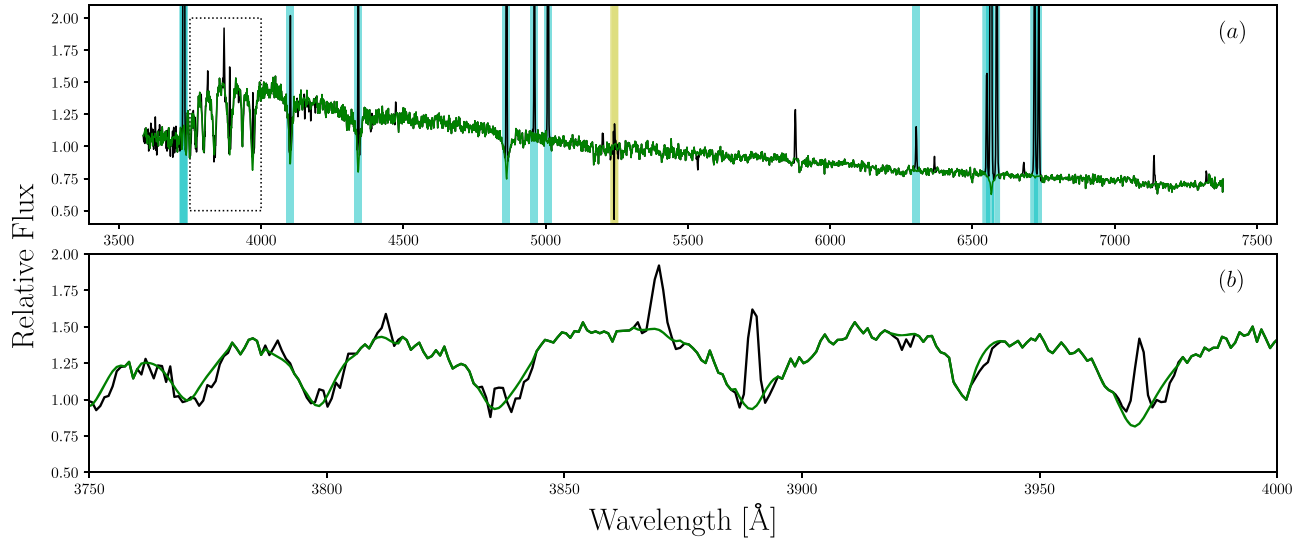

Figure 2. Rest-frame original spectrum for galaxy spec-0541-51959-0600 (black line) and the spectrum used for the stellar population template fitting (green line) that has gas emission lines, sky lines, and discrepant pixels masked. Panel (a) shows the entire wavelength range, panel (b) shows a close-up of the region covering the higher-order Balmer lines (indicated by a black-dotted box in panel (a)). The cyan regions are emission lines explicitly masked using the pPXF function `determine_goodpixels`, and the yellow region is the 5577 Å sky line that is also explicitly masked. Any remaining emission lines or discrepant pixels are identified and masked by the CLEAN function in pPXF, which iteratively rejects pixels that deviate more than 3σ from the best fit and refits until no further pixels are clipped (Cappellari et al. 2002). The higher-order Balmer lines are not explicitly masked, because not all spectra have emission in these regions. However, as shown in panel (b), the method used effectively identifies remaining emission lines and masks them, recovering the shape of the underlying absorption feature.

However, an alternative is to use sets of theoretical spectra for single-age and single-metallicity populations that allow a full spectral fitting approach using not just a limited number of absorption features but the whole spectrum, including the shape of the continuum. In addition to the MILES models by Vazdekis et al. (2010, 2015) used here, other widely used sets of theoretical spectra include Bruzual & Charlot (2003) and Binary Population and Spectral Synthesis (Eldridge et al. 2017; Stanway & Eldridge 2018). While these models do not account for emission from ionized gas, the issue of emission lines obscuring absorption features is less severe with a full spectral fitting method than for Lick indices, because the whole spectrum is used. We therefore use spectral fitting to approach the comparatively less well-studied field of stellar populations in SFGs.

Despite the different stellar population models used in this work (Vazdekis et al. 2010, 2015) and in Paper I, (Schiavon 2007; Thomas et al. 2011), there is good agreement between results from these models. McDermid et al. (2015) show that there is a tight relation between stellar population parameters derived using Lick indices and Schiavon (2007) models, and mass-weighted parameters derived from full spectral fitting and Vazdekis et al. (2010) models for ETGs. Their Figure 4 shows that the [Z/H] derived from the two models and methods closely follow the one-to-one relation. The ages follow a tight correlation offset from the one-to-one line, with the luminosity-weighted Schiavon (2007) ages being systematically younger than the mass-weighted Vazdekis et al. (2010) ages. However this is most likely a result of luminosity-weighted ages being more sensitive to young stars than mass-weighted ages (Serra & Trager 2007), rather than a difference in the models used. Additionally, Scott et al. (2017) showed that there is good agreement between the Schiavon (2007) and Thomas et al. (2011) models, differing most in the low-[Z/H] regime.

Our stellar population analysis consists of two main steps: Step 1 involves masking the spectra of emission and sky lines; Step 2 involves fitting the masked spectrum as a weighted sum of single-age and single-metallicity templates.

3.1. Step 1. Emission Line Masking

The aim of this preprocessing stage is to mask sky and gas emission lines. We begin by de-redshifting the galaxy and masking known sky and galaxy emission lines. Specifically, we use the function `determine_goodpixels` from the Python implementation of the publicly available Penalized Pixel-Fitting software (pPXF; Cappellari & Emsellem 2004; Cappellari 2017) to mask 13 common emission lines (see pPXF documentation for emission line details). Additionally, we also mask the sky line in the region between 5565 and 5590 Å. These masked regions are highlighted in panel (a) of Figure 2. We then perform two fits to the masked spectrum, using pPXF and all 985 empirical stellar templates from the MILES library (Sánchez-Blázquez et al. 2006a; Falcón-Barroso et al. 2011) broadened to the SDSS instrumental resolution. The purpose of the first fit is to obtain an estimate of the noise and uses the variance given by the SDSS pipeline. Based on the $\chi^2_{\rm reduced}$ of the first fit, we then rescale the variances to give $\chi^2_{\rm reduced} = 1$. The median rescaling value is 0.994 with a standard deviation of 0.079. With this slightly improved noise estimate, the second fit identifies any remaining bad pixels by iteratively rejecting pixels that deviate more than 3σ from the best fit, refitting until no further pixels are rejected (see Section 2.1 of Cappellari et al. (2002) and the CLEAN keyword in the pPXF documentation). Panel (b) of Figure 2 demonstrates that emission lines not explicitly masked, such as the higher-order Balmer lines, are identified and masked by the CLEAN iterative pixel rejection. The pixels identified as bad or containing emission lines are then replaced by the best-fit model from the second fit.

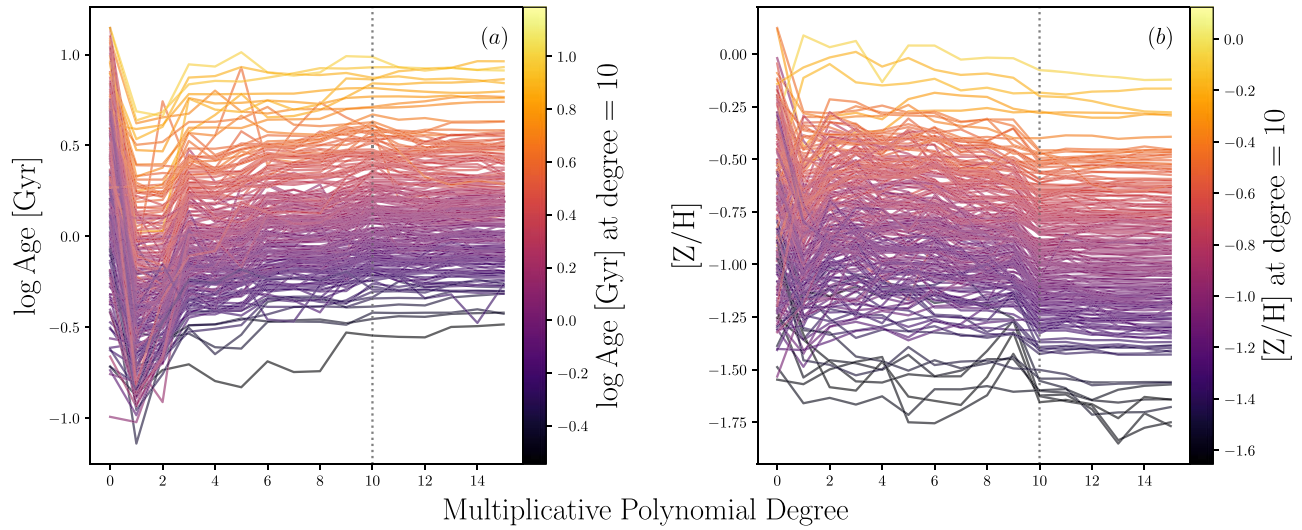

Figure 3. Luminosity-weighted age and [Z/H] from fits using varying degrees of the multiplicative polynomial, for a subsample of 209 galaxies. Each line is a single galaxy, and is colored by its age (panel (a)) and [Z/H] (panel (b)) from the 10th degree fit. The stellar population parameters vary little above a multiplicative polynomial of degree 10, hence, we use a 10th degree polynomial.

3.2. Step 2. Full Spectral Fitting

After the preprocessing stage, the stellar population age and metallicity are measured from the masked, emission-line-free spectrum. We fit the masked spectrum as a linear combination of synthetic single-population templates and a degree 10 multiplicative polynomial. The role of the multiplicative polynomial is to correct the shape of the continuum and account for dust extinction, however, it significantly increases the computation time (Cappellari 2017). Therefore, ideally the degree of the multiplicative polynomial should be the lowest value such that both residual flux calibration errors and dust extinction are corrected for. Using a randomly selected subsample of 209 galaxies (10% of the full sample) we tested the dependence of the resulting stellar population parameters on the degree of the multiplicative polynomial used. As shown in Figure 3, while the absolute values of age and [Z/H] vary greatly for fits with a multiplicative polynomial degree less than 10, the relative difference between galaxies remains similar. The stellar population parameters vary little for degree $\geqslant$10, hence, we use a degree 10 polynomial.

The templates used are from Vazdekis et al. (2010, 2015) and are constructed from the MILES stellar library and the base [α/Fe] BaSTI isochrones (Pietrinferni et al. 2004, 2006) and a Chabrier (2003) IMF. The base models contain no assumption on the abundance ratios, hence, the templates follow the abundance pattern of the Milky Way (Vazdekis et al. 2010). The 636 templates span an approximately regular grid in age and metallicity, spanning $-2.27 \leqslant [Z/H] \leqslant 0.40$ ($0.0001 \leqslant Z \leqslant 0.040$) and $0.03\,\mathrm{Gyr} \leqslant \mathrm{Age} \leqslant 14.0\,\mathrm{Gyr}$. We perform both luminosity-weighted (i.e., templates are individually normalized; Section 4) and mass-weighted fits (i.e no renormalization of templates; Section 5), however, we focus the analysis and discussion predominantly on the luminosity-weighted parameters. Given the galaxies in our sample are star forming, their spectra are dominated by young stars and so the contribution from low-luminosity old stars is not well constrained, making it harder to recover the true mass-weighted parameters. Each template is assigned a weight and from the combinations of weights a star formation history can be inferred (e.g., McDermid et al. 2015). However, the recovery of the star formation history is an ill-conditioned inverse problem without a unique solution unless further constraints are imposed (e.g., Press et al. 1987). This is because of the not-insignificant degeneracies between stellar spectra with different ages and metallicities. A common solution is to use linear regularization, which constrains the weights of neighboring templates (in age–metallicity space) to vary smoothly. While linear regularization produces more realistic star formation histories, typical degrees of regularization (see criterion advocated by Press et al. 1992 and used by, for example, McDermid et al. 2015; Norris et al. 2015; Boecker et al. 2020) are not expected to significantly change the weighted stellar population parameters, and we confirmed this to be the case for the luminosity-weighted age and [Z/H] using the random subsample of 209 galaxies. However, we did find a small systematic offset between the regularized and non-regularized parameters, in that the regularized values are on average 0.06 dex older and 0.07 dex more metal rich. This offset is introduced by regularizing over templates that are not evenly spaced in age or metallicity. The Vazdekis et al. (2010) templates have larger spacing at older ages, hence, smoothing between adjacent templates results in the regularized values being slightly older. This offset is small and less than the median uncertainties on the stellar population parameters ($\sigma_{\mathrm{logAge}} = 0.12$ dex and $\sigma_{[\mathrm{Z/H}]} = 0.10$ dex). Overall, we prefer to use the non-regularized fits in estimating the weighted ages and metallicities.

3.2.1. Estimating Uncertainties

We derive uncertainties on the luminosity-weighted stellar population parameters as a function of the median S/N per pixel, derived from testing performed on the same 209 galaxies used to test the degree of the multiplicative polynomial. First, we shuffle the residuals from the best fit within seven bins approximately 500 Å wide, and add this to the best-fit spectrum and refit, repeating 100 times per galaxy. The resulting stellar population parameter distribution is approximately Gaussian and centered around the original fit. Hence, we take the standard deviation of the distribution as the uncertainty on the stellar population parameter. Figure 4 shows the dependence of

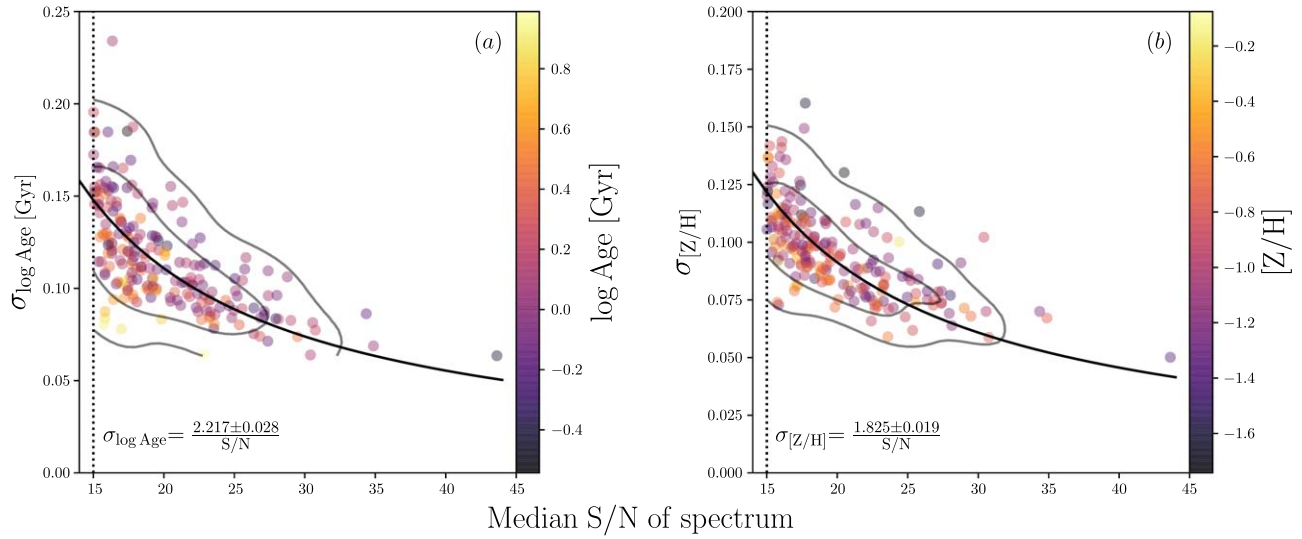

Figure 4. Uncertainty on luminosity-weighted age and [Z/H] versus the median S/N of the spectrum for the subsample of 209 test galaxies. Each point is colored by its age (panel (a)) and [Z/H] (panel (b)). The gray contours enclose 95% and 68% of the data. In both panels the black line is the best-fit inverse relation, which is then used to assign an uncertainty on age and [Z/H] to every galaxy in the full sample, based on its spectral S/N.

the measured uncertainty on the median spectral S/N for the 209 test galaxies. Both the uncertainty on age and [Z/H] show an inverse dependence on the S/N, which we fit using the Levenberg–Marquardt least-squares optimization algorithm implemented in Python by the `SciPy` package's `optimize.curve_fit` routine (Jones et al. 2001). We then use these relations, $\sigma_{\mathrm{logAge}} = \frac{2.217}{\mathrm{S/N}}$ and $\sigma_{[\mathrm{Z/H}]} = \frac{1.825}{\mathrm{S/N}}$, to assign uncertainties to the age and [Z/H] of each galaxy based on its S/N.

Unlike the luminosity-weighted parameters, the mass-weighted stellar population parameters do not show a strong variation with the S/N, and show greater scatter at a fixed S/N. Therefore, rather than assigning an uncertainty to each galaxy based on its S/N, we use the median uncertainties from the test subsample, $\sigma_{\mathrm{logAge}} = 0.096$ and $\sigma_{[\mathrm{Z/H}]} = 0.18$, and use these values for every galaxy in the sample.

4. Luminosity-weighted Ages and Metallicities

4.1. Fitting Method

We fit both two-parameter lines $z = a_0 + a_1 x$ and three-parameter planes $z = a_0 + a_1 x + a_2 y$ to the relationships between stellar population parameters (age and metallicity) and structural properties (M_*, R_e and the combinations Φ and Σ), allowing for intrinsic scatter in the z direction (i.e., in the stellar population parameter). These fits are performed using a Bayesian approach with uniform priors on the slope(s), intercept, and intrinsic scatter.

The posterior function is first optimized using the differential evolution numerical method (Storn & Price 1997), followed by Markov Chain Monte Carlo integration (Goodman & Weare 2010) of the posterior distribution to estimate the uncertainties on each model parameter using the Python package `emcee` (Foreman-Mackey et al. 2013).

For both the line and plane fits we quantify the residuals as a function of R_e, as displayed in the inset at the bottom right of each panel. In conjunction with the plane fit (where the residual correlation is close to zero by construction), the slopes of the residual correlations illustrate which of M_*, Φ, or Σ best encapsulates the stellar population parameter's dependence on size.

For each relation we use several metrics to quantify both the significance of the correlation and the tightness of the scatter about the fit. The Spearman and Pearson correlation coefficients (ρ_S, ρ_P) characterize the significance, while the root-mean-square (rms) scatter and median absolute deviation (*mad*) about the fit quantify the tightness. The absolute *intrinsic* scatter in the relations is difficult to measure, because it is sensitive to the assumed observational uncertainties. However, given the nonzero observational uncertainty on R_e, it follows that $M_* R_e^i$ necessarily has a higher total observational uncertainty than M_* alone (for $i \neq 0$). Moreover, if $M_* R_e^j$ shows less scatter than $M_* R_e^i$ for $j > i$, $M_* R_e^j$ must be intrinsically tighter. Hence, by understanding the relative observational uncertainties, we can compare the measured scatter about the fits and rank the relations based on their relative intrinsic scatter. The colorscales in the figures show log R_e, smoothed using the locally weighted regression algorithm LOESS (Cleveland & Devlin 1988; Cappellari et al. 2013), to highlight the residual trends with galaxy size.

4.2. Metallicity [Z/H]

We show the results of this analysis for [Z/H] in Figure 5. Of the three structural parameters, [Z/H]–Φ in panel (c) has the tightest correlation. Indeed, the plane fit in panel (a) shows that the optimum coefficient of log R_e is -1.02 ± 0.16, consistent within the uncertainties to the -1 coefficient corresponding to Φ. Furthermore for the [Z/H]–Φ relation, the σ_{int}, rms, and *mad* are all consistent within the uncertainties to the plane fit. Moving from left to right in Figure 5 from M_* (panel (b)) through Φ (panel (c)) to Σ (panel (d)), we see a peak in ρ_P and ρ_S, as well as a minimum in σ_{int}, rms, and *mad* at Φ (panel (c)). Invoking the argument given above, the larger *observational* uncertainties in [Z/H]–Φ compared to [Z/H]–M_*, along with slightly less scatter, implies [Z/H]–Φ must have less *intrinsic* scatter than [Z/H]–M_*.

In addition to the tightness of the fits, the residual trends with log R_e indicate which of the parameters investigated best encapsulates the dependence of [Z/H] on size. The [Z/H]–M_* diagram in panel (b) and the [Z/H]–Σ diagram in panel (d)

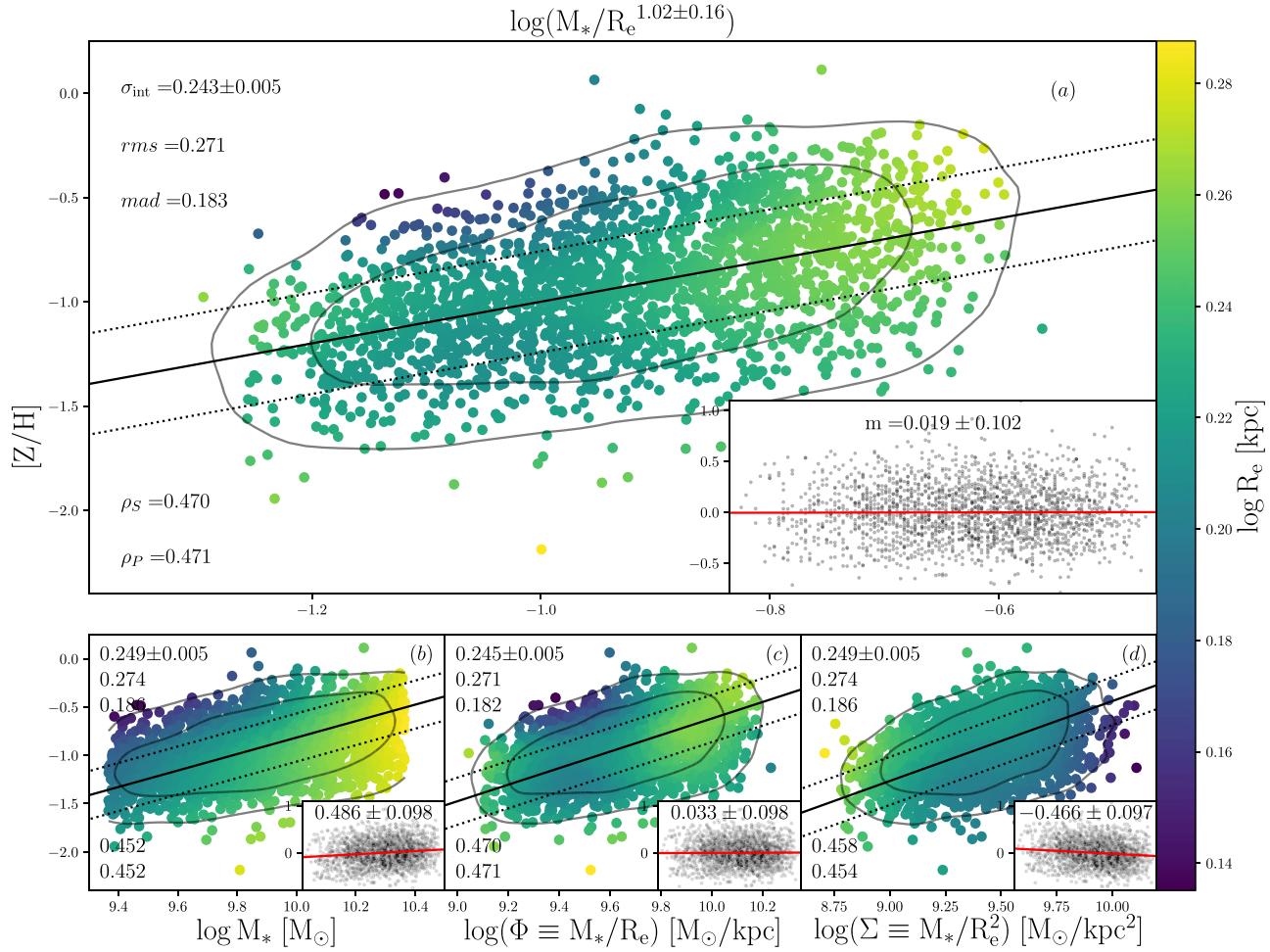

Figure 5. Luminosity-weighted [Z/H] versus the best-fit linear combination of M_* and R_e (panel (a)) and luminosity-weighted [Z/H] versus M_*, $\Phi \equiv M_*/R_e$ and $\Sigma \equiv M_*/R_e^2$ (panels (b)–(d)). In each panel the solid black line is the best-fit linear relation and the dashed lines indicate the intrinsic scatter $\sigma_{\rm int}$ about this fit. The colorscale indicates the LOESS-smoothed value of $\log R_e$ (in kpc). The scatter, both rms and *mad*, is given at the top left of each panel and the correlation coefficient, both Superman ρ_S and Pearson ρ_P, is given at the bottom left. The contours enclose 68% and 95% of the sample. The insets show the best-fit residuals versus $\log R_e$; the slope of the residual trend m is displayed at the top of each inset. Panels (a) and (c) indicate that of the three structural parameters studied, [Z/H] correlates best with Φ.

both show significant residual trends with size. As shown by the inset panels, the slopes of the residuals of [Z/H]–M_* and [Z/H]–Σ with size are $m = 0.486 \pm 0.098$ and $m = -0.466 \pm 0.097$, respectively. On the other hand, the [Z/H]–Φ relation shows no residual trend with size ($m = 0.033 \pm 0.098$). This lack of residual trend with size indicates that Φ best encapsulates the relative dependence of [Z/H] on mass and size.

The results are quantitatively unchanged if we instead use M_* from Chang et al. (2015). The plane fit using M_* from Chang et al. (2015) is $[Z/H] \propto M_*/R_e^{1.00\pm0.13}$, consistent within the uncertainties to our presented results $[Z/H] \propto M_*/R_e^{1.02\pm0.16}$ using M_* from Kauffmann et al. (2003a).

4.3. Age

In Figure 6, panels (b)–(d) show the relations between age and M_*, Φ, and Σ, while panel (a) shows age fitted by a plane in M_* and R_e. For the plane fit, the optimum coefficient of $\log R_e$ is -1.97 ± 0.18, consistent within the uncertainties to the -2 coefficient corresponding to Σ, indicating that despite the high intrinsic scatter and observational uncertainties, age scales most closely with surface mass density Σ. Indeed the improvement of the plane fit (panel (a)) over the age–Σ relation (panel (d)) is marginal, as indicated by the identical values of ρ_S and ρ_P. Moving from left to right in Figure 6 from M_* (panel (b)) through Φ (panel (c)) to Σ (panel (d)), we see a consistent decrease in the scatter, rms, *mad*, and residual slope, along with a corresponding increase in ρ_P and ρ_S. Given the higher observational uncertainty of Σ compared to M_* or Φ, the tighter correlation with Σ implies a fundamentally closer relationship.

Both the age–M_* (panel (b)) and age–Φ (panel (c)) relations show significant positive residual trends with size, $m = 0.819 \pm 0.097$ and $m = 0.458 \pm 0.098$, respectively, whereas the age–Σ residuals (panel (d)) show no trend with size ($m = 0.007 \pm 0.093$). This lack of residual trend with size indicates that Σ best encapsulates the relative dependence of age on mass and size.

If we instead use M_* from Chang et al. (2015) rather than that from Kauffmann et al. (2003a), our results remain quantitatively unchanged. The plane fit using M_* from Chang et al. (2015) is age $\propto M_*/R_e^{1.90\pm0.16}$, consistent within the uncertainties to age $\propto M_*/R_e^{1.97\pm0.18}$ using M_* from Kauffmann et al. (2003a).

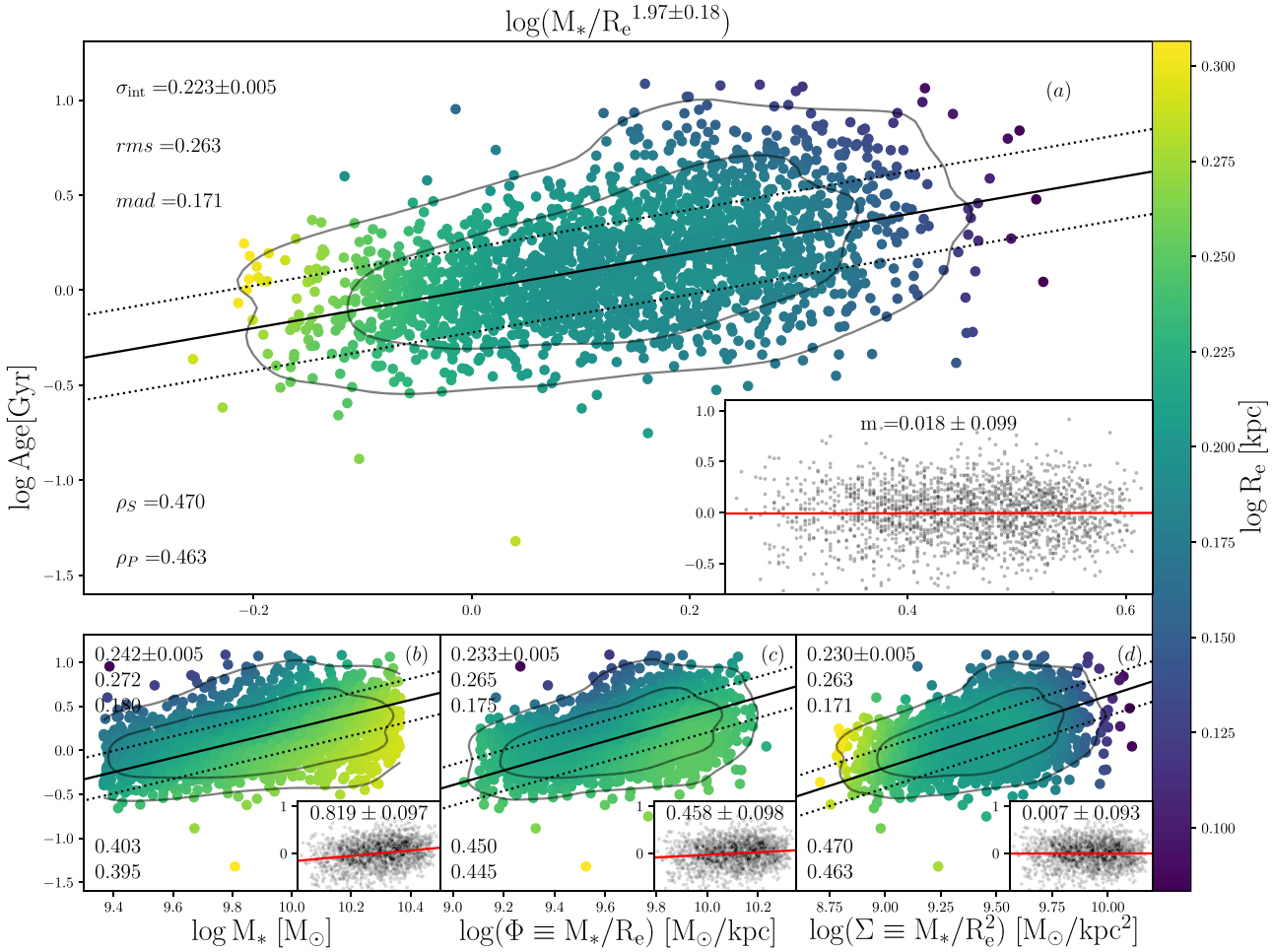

Figure 6. Luminosity-weighted age versus the best-fit linear combination of M_* and R_e (panel (a)), and luminosity-weighted age versus M_*, $\Phi \equiv M_*/R_e$ and $\Sigma \equiv M_*/R_e^2$ (panels (b)–(d)). In each panel the solid black line is the best-fit linear relation and the dashed lines indicate the intrinsic scatter $\sigma_{\rm int}$ about this fit. The colorscale indicates the LOESS-smoothed value of $\log R_e$ (in kpc). The scatter, both rms and *mad*, is given at the top left of each panel and the correlation coefficient, both Spearman ρ_S and Pearson ρ_P, is given at the bottom left. The contours enclose 68% and 95% of the sample. The insets show the best-fit residuals versus $\log R_e$; the slope of the residual trend m is displayed at the top of each inset. Panels (a) and (d) indicate that of the three structural parameters studied, age correlates best with Σ.

5. Mass-weighted Ages and Metallicities

Here we present the mass-weighted stellar population measurements and analyze their dependence on mass and size, to investigate whether the results presented for the luminosity-weighted parameters ($[Z/H]_L$ and age_L) in Section 4 hold when using mass-weighted parameters ($[Z/H]_M$ and age_M). Unlike $[Z/H]_L$ and $logage_L$, which show linear dependencies on log M_*, log Φ, and log Σ, both $[Z/H]_M$ and $logage_M$ show a nonlinear dependence on these parameters. We are therefore unable to apply to the mass-weighted parameters the linear fitting method (described in Section 4) that we used for the luminosity-weighted parameters. Instead, we analyze the dependence of the mass-weighted parameters on log M_*, log Φ, and log Σ by showing how $[Z/H]_M$ and $logage_M$ vary in the mass–size plane.

First, in Figure 7 we compare the mass-weighted and luminosity-weighted parameterizations for both our sample of SFGs and an additional sample of ETGs. For the early types, we use an aperture-matched subsample (following the same criteria described in Section 2.1) of 1266 galaxies from the MOrphologically Selected Early types in SDSS (MOSES; Schawinski et al. 2007a; Thomas et al. 2010) catalog. Similarly, Figure 4 of McDermid et al. (2015) compares mass-weighted [Z/H] and age derived from full spectral fitting to single stellar population (SSP) parameters measured from Lick indices for ETGs from the ATLAS^{3D} survey (Cappellari et al. 2011). Given that SSP parameters are expected to closely follow luminosity-weighted parameters (Serra & Trager 2007), we compare our results with those of McDermid et al. (2015).

We then show how the the mass-weighted parameters depend on mass and size by how they vary in the mass–size plane (Figure 8 for [Z/H] and Figure 9 for age). We include the luminosity-weighted parameters in Figures 8 and 9 for reference. To visually highlight the underlying trends we use the LOESS (Cleveland & Devlin 1988; Cappellari et al. 2013) algorithm. We compare our luminosity-weighted mass–size planes to similar figures by Scott et al. (2017) and Li et al. (2018). Specifically, we compare to Figures 9 and 10 of Scott et al. (2017), which show how SSP parameters for SAMI galaxies vary in the mass–size plane, and Figure 4 of Li et al. (2018), who show how luminosity-weighted parameters vary in the mass–size plane for galaxies from the Mapping Nearby Galaxies at APO (MaNGA; Bundy et al. 2015) survey.

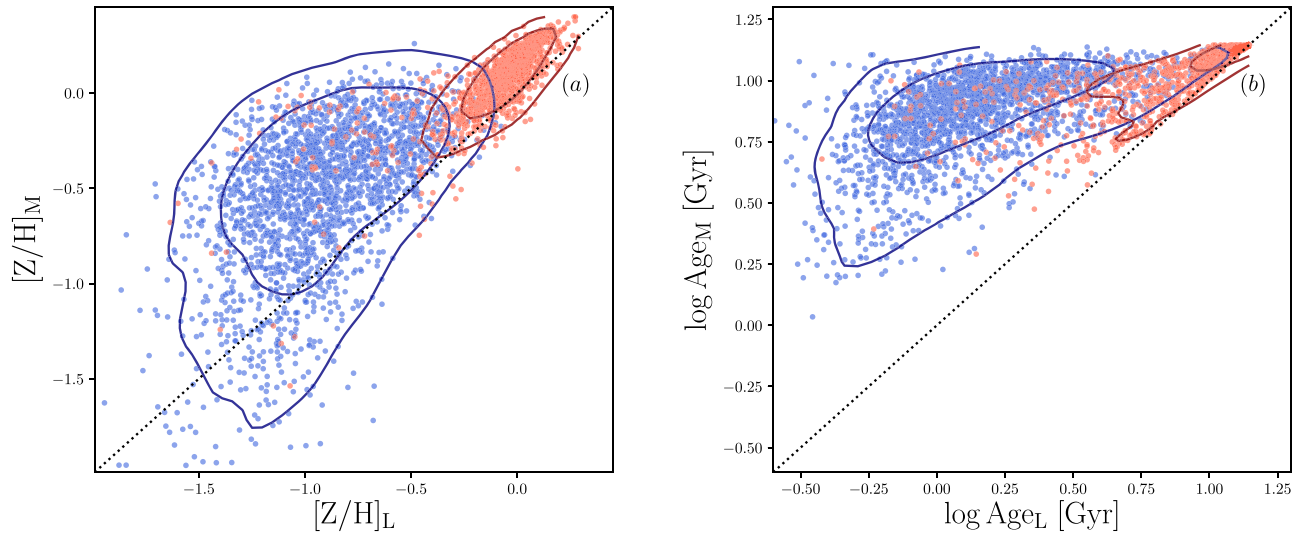

Figure 7. Comparison of mass-weighted and luminosity-weighted [Z/H] (panel (a)) and age (panel (b)). Blue points are SFGs, red points are ETGs from the MOSES catalog. The black-dotted line shows the 1–1 relation. The contours enclose enclose 68% and 95% of each sample.

5.1. Metallicity [Z/H]

Luminosity-weighted metallicity depends mostly on the old stellar population (Serra & Trager 2007), and so we expect good agreement between $[Z/H]_L$ and $[Z/H]_M$. For early types (red points in Figure 7(a)) there is a clear 1–1 relation, although unlike Figure 4 of McDermid et al. (2015) there is a small zero-point offset, with $[Z/H]_M$ being on average 0.16 dex more metal rich than $[Z/H]_L$. However this 1–1 relation appears limited to above $[Z/H]_L \approx -0.5$, below which there is a significant bend seen strongly in the SFGs (blue points). In addition to not being 1–1, there is a large variation in $[Z/H]_M$ at fixed $[Z/H]_L$ for the SFGs.

Despite the nonlinearity between $[Z/H]_M$ and $[Z/H]_L$, we see in Figure 8 that for SFGs, $[Z/H]_M$ (panel (b)), like $[Z/H]_L$ (panel (a)), follows lines of constant Φ. Li et al. (2018) also showed that $[Z/H]_L$ for spiral galaxies in MaNGA varies along lines of constant Φ, and Scott et al. (2017) showed that for all morphological types $[Z/H]_{SSP}$ varies along lines of constant Φ. This strengthens our quantitative results that global stellar metallicity is strongly dependent on the gravitational potential of the galaxy.

5.2. Age

It is well established that luminosity-weighted ages (age_L) strongly trace the younger stars (Trager et al. 2000; Serra & Trager 2007; Trager & Somerville 2009), and indeed we see in panel (b) of Figure 7 that for both the ETGs and SFGs, age_M is consistently older than age_L. The early types (red) resemble the relation shown in Figure 4 of McDermid et al. (2015), but for the SFGs (blue) there is a large spread in the age_M at fixed age_L. Notably, even at the youngest age_L, there are galaxies reaching the upper limit of the templates for age_M. For the youngest luminosity-weighted galaxies, it is possible that for these galaxies the spectrum is so dominated by young stars the contribution from low-luminosity old stars is poorly constrained, resulting in over-fitting of the oldest templates. This then leads to the large spread of age_M at fixed age_L.

Figure 9 shows that age_M (panel (b)) appears to follow lines of constant Σ, although not as closely as age_L. Age_M appears to vary more steeply than age_L, at a rate somewhere between lines of constant Φ and Σ, although for small, low-mass galaxies (below a stellar mass of $\approx 10^{9.7} M_\odot$ and radius $\approx 10^{0.2}$ kpc) age_M appears to closely follow Σ. Scott et al. (2017) showed that age_{SSP} also varies approximately along lines of constant Σ. While Li et al. (2018) do not plot lines of constant Σ, from their Figure 4 it is clear age_L varies more shallowly than the lines of constant Φ (lines of constant Σ are more shallow than lines of constant Φ).

6. Discussion

Our aim was to investigate which parameter (mass M_*, gravitational potential $\Phi \sim M_*/R_e$, or surface density $\Sigma \sim M_*/R_e^2$) best predicts the stellar population properties (age and metallicity) of SFGs. Looking both at the luminosity-weighted (Section 4) and mass-weighted (Section 5) parameters and taking into account both the tightness of the relations and any residual trends with galaxy size, we find age correlates best with surface density while metallicity [Z/H] correlates best with gravitational potential. These results are in striking agreement with Paper I, where, using different methods to determine stellar population parameters, we found ETGs also show age correlating best with Σ and [Z/H] correlating best with Φ. We note that "quiescent/star forming" refers to a classification based on specific SFR whereas "early type/late type" refers to a morphological classification, so "early type" and "star forming" are not mutually exclusive categories (see Section 1 for further discussion of the overlap). However given the pronounced differences in internal structure, kinematics, and stellar population properties between the two categories, it is significant that they exhibit the same scaling relations. Crucially, this indicates that the dominant mechanism(s) driving stellar population evolution must originate while galaxies are still star forming, and must be (at least) preserved through mergers and quenching processes. Here we discuss various mechanisms that could lead to these scaling relations.

6.1. Origin of the Metallicity–Potential Relation

We have demonstrated that global *stellar* metallicity exhibits a tight correlation with the gravitational potential for both ETGs (Paper I) and SFGs (Paper II). D'Eugenio et al. (2018)

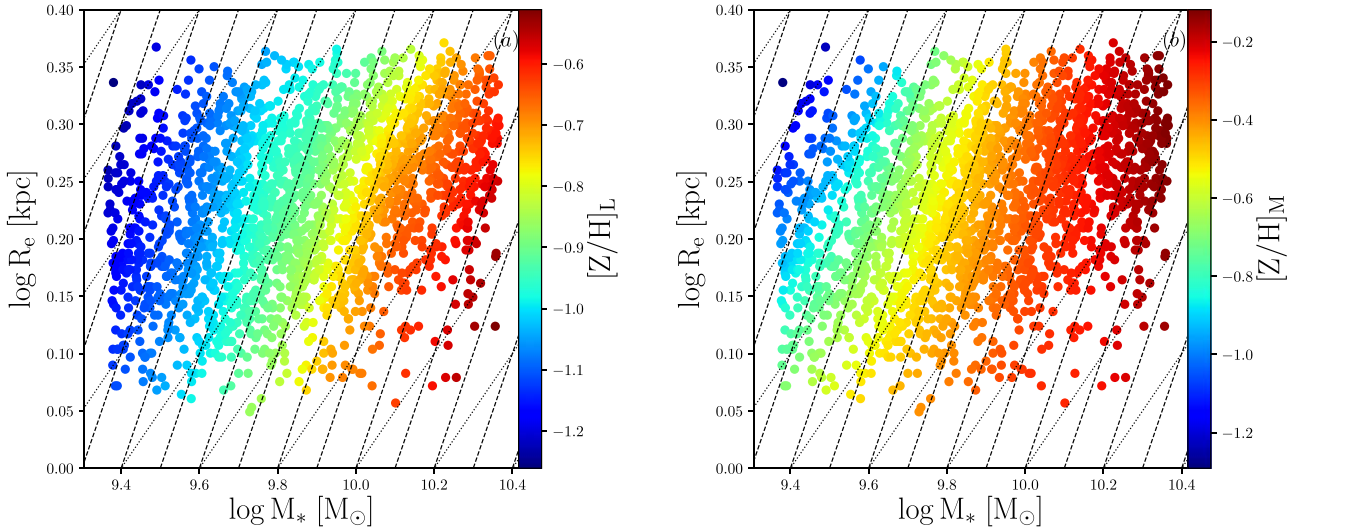

Figure 8. Mass–size plane for our sample of SFGs, with the colorscale representing LOESS-smoothed luminosity-weighted metallicity ($[Z/H]_L$; panel (a)) and mass-weighted metallicity ($[Z/H]_M$; panel (b)). The dashed lines are lines of constant $\Phi \propto M_*/R_e$, and the dotted lines are lines of constant $\Sigma \propto M_*/R_e^2$. Both $[Z/H]_M$ and $[Z/H]_L$ follows lines of constant Φ.

found the same result for global *gas-phase* metallicity in SFGs. Furthermore, recent works hint at the existence of a similar global relation at higher redshift. Díaz-García et al. (2019) showed that at $z \sim 1$ more compact quiescent galaxies are both older and more metal rich than their diffuse counterparts at fixed mass.

In general, total metal content is a reflection of the number of generations of stars the galaxy has formed. However, we can rule out the [Z/H]–Φ relation being driven simply by the number of stellar generations, due to the existence of a strong correlation between the star formation duration (via either $[\alpha/Fe]$ or the e-folding timescale) and gravitational potential in both early types (M/R_e: Paper I; σ: Nelan et al. 2005; Thomas et al. 2005, 2010; Robaina et al. 2012; McDermid et al. 2015; Scott et al. 2017) and late types (Ganda et al. 2007), since galaxies with a shallower potential (lower σ) have *longer*, rather than shorter, star formation durations.

The existence of the [Z/H]–Φ relation in both the gas and stars, in both young SFGs and old early types, indicates the relation originates with in situ star formation, and is maintained throughout ex situ assembly. Although the radius to which we probe ($\sim 1R_e$) is dominated by in situ stars (Pillepich et al. 2014; Cook et al. 2016; Greene et al. 2019), we explore mechanisms related to both in situ and ex situ formation to explain the presence of the metallicity–potential relation. Regarding in situ formation, either low-Φ galaxies *lose a higher fraction* of their metals or low-Φ galaxies *produce less* metals. In the following discussion we explore two possibilities, namely: (1) low-Φ galaxies are more likely to lose more metals, due to the relation between gravitational potential and gas escape velocity; or (2) low-Φ galaxies produce less metals due to variations in the IMF. We then discuss how the relation could be preserved in galaxy mergers.

6.1.1. Metallicity Determined by Gas Escape Velocity?

In Paper I we proposed that the metallicity–potential relation is driven by low-Φ galaxies being more likely to lose their metals due to the relation between gravitational potential and gas escape velocity. The depth of the gravitational potential sets the escape velocity for ejection from the galaxy for metal-rich gas expelled by supernovae. This dependence of the gas escape velocity on the gravitational potential also explains the existence of metallicity gradients within galaxies: the gravitational potential decreases outwards in galaxies, allowing stellar feedback to more easily eject metals in the outskirts than in the center (Cook et al. 2016) and leading to decreasing radial stellar metallicity gradients, as observed in both late-type galaxies (Sánchez-Blázquez et al. 2014) and ETGs (e.g Goddard et al. 2017; Martín-Navarro et al. 2018; Ferreras et al. 2019). This interpretation is supported by the results of Scott et al. (2009), who found a strong correlation in early types between *local* [Z/H] and *local* escape velocity derived from dynamical models. Møller & Christensen (2020) also show that halo gas-phase metallicities are well explained by a dependence of the local gas-phase metallicity on the local gravitational potential. Supporting this explanation, simulations show that steep stellar population gradients are the result of in situ star formation (Pipino et al. 2010), and mergers then tend to diminish these gradients (Kobayashi 2004; Di Matteo et al. 2009), particularly at large radii where the stars have predominantly ex situ origins (Hirschmann et al. 2015).

A test of this hypothesis is how the metallicity of the circumgalactic medium (CGM) correlates with galaxy structure; logically this mechanism should lead to a relative enrichment of the CGM around low-Φ galaxies at fixed M_*. Due to the low-density nature of the CGM, obtaining precise metallicity measurements is time-consuming, and recent studies have sample sizes of less than 50 galaxies (e.g., Prochaska et al. 2017; Pointon et al. 2019). In addition, because the CGM is composed not only of stellar ejecta but also pristine gas from the halo and low-metallicity gas from satellites (e.g., Shen et al. 2013), any trend with galaxy gravitational potential would be difficult to interpret. An alternative way forward might be to investigate the dependence of CGM metallicity on galaxy structure in large-scale cosmological simulations of galaxy formation.

6.1.2. Metallicity Determined by IMF?

Another explanation for low-Φ galaxies producing fewer metals could be variations in the types of stars formed, i.e., the

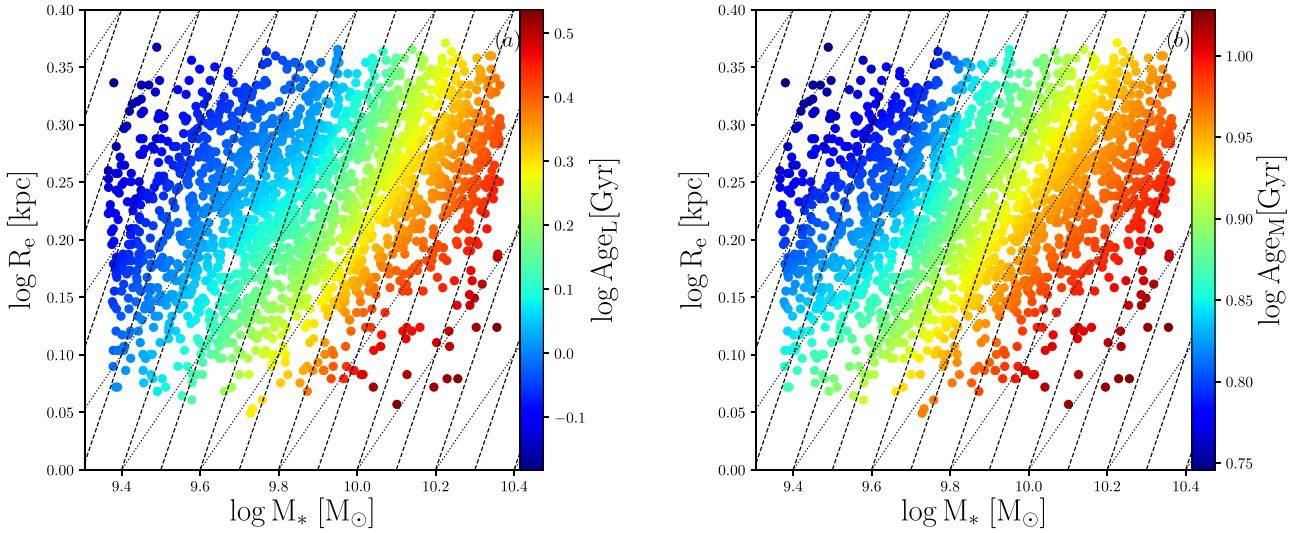

Figure 9. Mass–size plane for our sample of SFGs, with the colorscale representing LOESS-smoothed luminosity-weighted age (age_L; panel (a)) and mass-weighted age (age_M; panel (b)). The dashed lines are lines of constant $\Phi \propto M_*/R_e$ and the dotted lines are lines of constant $\Sigma \propto M_*/R_e^2$. While age_L follows lines of constant Σ, age_M instead varies somewhere between lines of constant Φ and Σ.

IMF. Different stellar types produce different chemical yields, and combined with their varying lifespans, affect both total metallicity [Z/H] and α-enhancement, with higher-mass stars leading to higher metallicities and α-enhancements (see e.g., Matteucci 2012). Indeed, Vincenzo et al. (2016) showed that the more top-heavy IMFs (Kroupa 2001; Chabrier 2003), with their greater proportion of high-mass stars, lead to twice the oxygen yields of the standard Salpeter (1955) IMF. Furthermore there is mounting evidence for a varying IMF both between (e.g., van Dokkum & Conroy 2010; Cappellari et al. 2012; Conroy & van Dokkum 2012; Spiniello et al. 2014; Li et al. 2017) and within galaxies (Martín-Navarro et al. 2015a; van Dokkum et al. 2017; Parikh et al. 2018; Vaughan et al. 2018), although exactly what drives these variations remains unclear.

On the other hand, metallicity has been suggested to *anticorrelate* with the relative number of high-mass stars, both globally (Marks et al. 2012) with [Fe/H] and locally (Martín-Navarro et al. 2015b) with total metallicity [Z/H]. However in contrast, recent works have found that while both metallicity and IMF vary radially, spatially resolved maps show that IMF variations do not follow total metallicity [Z/H] variations (Martín-Navarro et al. 2019). Given these results, while the IMF clearly plays an important role in overall metal production, we find IMF variations do not explain the global metallicity–potential relation.

6.1.3. Ex situ Preservation

In addition to the previously discussed *generative* in situ mechanisms, in order for the metallicity–potential relation to persist in ETGs it must be *preserved* during galaxy mergers. While simulations show that mergers tend to diminish metallicity gradients (Kobayashi 2004), it is possible that the global relation is preserved due to the compactness of a satellite influencing where it accretes onto the host. Using *N*-body simulations, both Boylan-Kolchin & Ma (2007) and Amorisco (2017) show that a compact, high-density satellite is more likely to accrete into the center of the host, whereas a diffuse, low-density satellite is more easily disrupted by dynamical friction and therefore accretes onto the host's outskirts. This differential process acts to reinforce the already established in situ metallicity–potential relation: compact, high-Φ satellites will have relatively high metallicity and deposit their high-metallicity material into the center of the host, increasing the host's gravitational potential. Conversely, diffuse, low-Φ satellites will deposit low-metallicity material at large radii, decreasing the host's gravitational potential at fixed mass. Additionally, Scott et al. (2013) found that, despite their different merger histories, both fast and slow rotating ETGs lie on the same scaling relation between the Mg*b* spectral index and local escape velocity V_{esc}. They showed that simple model parameterizations indicate dry major mergers should move galaxies off, not along, the relation, and so the intrinsic scatter in the relation therefore provides an upper estimate on the frequency of dry major mergers. Combining predictions from *N*-body binary mergers and the observed scatter about the Mg*b*–V_{esc} relation, they estimated a typical present-day ETG to have typically only undergone about 1.5 dry major mergers.

Future studies comparing the slope of the metallicity–potential relation over all galaxy types, at low and high redshift, could further reveal the relative importance of these in situ and ex situ mechanisms, and the precise extent to which mergers diminish or preserve the relation.

6.2. Origin of the Age–Σ Relation

We find stellar age correlates best with surface mass density Σ for both SFGs and ETGs (Paper I). While the true average stellar population age depends on when the galaxy first formed, the rate of star formation, and when the galaxy quenched, in practice single-burst model ages strongly depend on the age of the youngest stars (Trager et al. 2000; Serra & Trager 2007; Trager & Somerville 2009). In Paper I we proposed two possible explanations for the age–Σ relation in ETGs: (1) as a fossil record of the $\Sigma_{SFR} \propto \Sigma_{gas}$ relation while forming stars, or (2) as a result of compactness-driven quenching mechanisms.

For ETGs these two scenarios are completely degenerate, but in this work, because we use SFGs, we are able to break this degeneracy. In fact, given the result of this paper that the age–Σ relation also exists in SFGs, it would be an odd coincidence if the same relation was due to completely different physical

processes. Assuming therefore the mechanism(s) leading to this relation is (are) the same for ETGs and SFGs, the relation must originate *before* quenching. Nonetheless, certain quenching mechanisms may further emphasize the relation. Here we discuss mechanisms related to each of these phases that could lead to or reinforce the age–Σ relation. First we explore whether galaxies that formed earlier have high-Σ due to higher gas densities in the early universe, building upon the hypothesis from Paper I that the relation is a fossil record of the $\Sigma_{\rm SFR} \propto \Sigma_{\rm gas}$ relation. We then discuss the possibility that compact galaxies quench earlier.

6.2.1. Compact Galaxies Formed Earlier?

The age–Σ relation could be a result of more compact galaxies having formed earlier, because higher gas fractions in the early universe mean galaxies formed more compactly during their in situ formation phase (Wellons et al. 2015). While this mechanism would apply to both SFGs and ETGs, we first consider the body of evidence related to ETGs, then consider how this also affects SFGs.

The current paradigm from both observations and simulations is that present-day ETGs underwent two main phases of evolution: an early period of intense in situ star formation at $z\sim$ 2, producing the very compact galaxies observed at high redshift (e.g., van Dokkum et al. 2008; van der Wel et al. 2008), followed by passive ex situ buildup via frequent minor and occasional major mergers (e.g., Oser et al. 2010; Barro et al. 2013; Rodriguez-Gomez et al. 2016; Wellons et al. 2016). During the in situ phase the high gas density leads to a high SFR density, a causation parameterized by the Kennicutt–Schmidt relation (Schmidt 1959; Kennicutt 1998; see Kennicutt & Evans 2012 for a review). As previously discussed in Paper I, the Kennicutt–Schmidt relation, $\Sigma_{\rm SFR} \propto \Sigma_{\rm gas}$, in SFGs naturally leads to an age–Σ_* relation. A high gas density causes a high SFR density, and assuming a non-replenishing gas supply, quickly exhausts the available gas, leading to a short star formation duration and an old stellar population. Over time, the original high gas density is converted into a high stellar mass density. In addition, Tacconi et al. (2013) showed that the Kennicutt–Schmidt relation is near linear from redshifts $z \sim$ 1–3, indicating this affects both old and young galaxies. Indeed, Franx et al. (2008) showed that specific SFR tightly anticorrelates with surface mass density (tighter than mass alone), concluding that star formation history is strongly dependent on surface mass density. Paper I also showed that [α/Fe], a proxy for star formation duration, correlates tightly with Σ (and Φ). Although still star forming, this fossil record of $\Sigma_{\rm SFR} \propto \Sigma_{\rm gas}$ is already detectable in our sample of SFGs as the age–Σ relation. Given the mass range of our sample of SFGs, $10^{9.4} < M_*/M_\odot < 10^{10.4}$, enough of the galaxies' star-forming period has passed for the relation with stellar age to be detectable. While the luminosity-weighted ages of SFGs are young, as discussed in Section 5.2, luminosity-weighted ages predominantly trace the youngest stars, and the stellar population overall is likely much older as indicated by the mass-weighted ages, which are significantly older.

Additionally, at low redshift, SFGs are larger than quiescent galaxies at fixed mass (Shen et al. 2003; Trujillo et al. 2007; Cimatti et al. 2008; Kriek et al. 2009; Williams et al. 2010; Wuyts et al. 2011; van der Wel et al. 2014; Whitaker et al. 2017), indicating that currently SFGs are different from the progenitors of present-day compact quiescent galaxies, and will evolve into extended quiescent galaxies (Barro et al. 2013). This explains both why old SFGs are more compact than young SFGs, and also why early types are more compact than SFGs. In this scenario, the age–Σ relation is a reflection of the gas density of the universe when the galaxy formed. We note, however, that any mechanism that causes a high gas density would also produce an age–Σ relation.

6.2.2. Compact Galaxies Quench Earlier?

In Paper I we proposed that the age–Σ relation in ETGs might be a result of compactness-driven quenching mechanisms. However, given the result of this work that age correlates tightly with Σ also for SFGs, we assume the mechanism(s) leading to the age–Σ relation is (are) the same for both quiescent and SFGs. Therefore, we infer the relation arises *before* quenching, thus disfavoring models where the relation is purely due to quenching. Nonetheless, quenching processes may act to reinforce an already-existing relation.[5] Further work quantitatively comparing the age–Σ relation in low redshift samples of quiescent galaxies and SFGs may help resolve whether the relations originate from the same mechanism(s).

Star formation history and quiescence, as quantified in a variety of ways, correlate strongly with compactness and the presence of a central bulge, both at low (Kauffmann et al. 2003b, 2004; Bell 2008; Franx et al. 2008; van Dokkum et al. 2011; Bluck et al. 2014; Omand et al. 2014; Woo et al. 2017) and high redshifts (e.g., Wuyts et al. 2011; Bell et al. 2012; Cheung et al. 2012; Szomoru et al. 2012; Lang et al. 2014). Woo et al. (2015) proposed two main quenching pathways that may act concurrently: rapid central compactness-related processes and prolonged halo (environmental) quenching. Compactness-related quenching mechanisms include processes that both build the central bulge and (either directly or indirectly) contribute to quenching, such as mergers and gaseous inflows from the disk. Specifically, gaseous inflows from the disk to the bulge, triggered by disk instability or an event such as a merger, are exhausted in a starburst, leading to increased bulge compactness. Additionally, these inflows can trigger active galactic nuclei which, if aligned with the gas disk, can cause molecular outflows, depleting surrounding gas on timescales of a few Myr and preventing further star formation (García-Burillo et al. 2014; Sakamoto et al. 2014). More recently, Woo & Ellison (2019) showed that, in addition to these compactness-related mechanisms, processes unrelated to central density such as secular inside-out disk growth (Lilly & Carollo 2016) combined with slow environmental quenching also naturally lead to a relation between the compactness of the galaxy (which they define by the surface mass density within the central 1 kpc, $\Sigma_{\rm 1kpc}$) and quiescence (defined by low sSFR). This compactness–quiescence relation would then naturally lead to a relation between surface mass density and stellar age in passive galaxies.

7. Summary

In this work we have used two- and three-dimensional fits to study how the age and metallicity [Z/H] of the global stellar population in SFGs correlate with the galaxy structural

[5] In principle, quenching could still be responsible for the observed trend if most SFGs had undergone a quenching phase, followed by rejuvenation. In practice, however, rejuvenation is not common and most SFGs have extended star formation histories (e.g., Thomas et al. 2010; Chauke et al. 2019).

parameters stellar mass (M_*), gravitational potential ($\Phi \sim M_*/R_e$), and surface mass density ($\Sigma \sim M_*/R_e^2$). This new study builds on our results for ETGs (Paper I). For both ETGs and SFGs, we find the tightest correlations and least residual trend with galaxy size for the age–Σ and [Z/H]–Φ relations. Finding these trends in both these studies, despite the different samples, methods, and models used to derive not only the stellar population parameters but also the stellar masses and effective radii, suggests our results are robust. We discuss multiple mechanisms that might produce these relations. We suggest that the [Z/H]–Φ relation is driven by low-Φ galaxies losing more of their metals because the escape velocity required by metal-rich gas to be expelled by supernova feedback is directly proportional to the depth of the gravitational potential. This relation is preserved during mergers, as elucidated by simulations. We rule out the possibility of the [Z/H]–Φ relation being due to IMF variations. In Paper I we discussed compactness-related quenching mechanisms that could lead to the age–Σ relation, however, given that in this work we show that the relation exists also in SFGs, it must arise *before* quenching. We therefore explore the possibility that the age–Σ relation is a result of compact galaxies forming earlier. Additionally, certain compactness-related quenching mechanisms may act to reinforce the already-existing relation. Future studies using cosmological simulations may help resolve the relative importance of each of these mechanisms.

T.M.B. is supported by an Australian Government Research Training Program Scholarship. N.S. acknowledges support of an Australian Research Council Discovery Early Career Research Award (project DE190100375) funded by the Australian Government. This research was supported by the Australian Research Council Centre of Excellence for All Sky Astrophysics in 3-Dimensions (ASTRO 3D), through project CE170100013. F.D.E. acknowledges funding through the H2020 ERC Consolidator Grant 683184. We thank the referee for constructive comments.

We made extensive use of the Python programming language and IPython extension (Perez & Granger 2007) and packages NumPy (van der Walt et al. 2011), SciPy (Jones et al. 2001), Astropy (Astropy Collaboration et al. 2013), and matplotlib (Hunter 2007). In preliminary analyses, we also used TOPCAT (Taylor 2005).

Funding for the SDSS and SDSS-II has been provided by the Alfred P. Sloan Foundation, the Participating Institutions, the National Science Foundation, the U.S. Department of Energy, the National Aeronautics and Space Administration, the Japanese Monbukagakusho, the Max Planck Society, and the Higher Education Funding Council for England. The SDSS website is located at http://www.sdss.org/.

The SDSS is managed by the Astrophysical Research Consortium for the Participating Institutions. The Participating Institutions are the American Museum of Natural History, Astrophysical Institute Potsdam, University of Basel, University of Cambridge, Case Western Reserve University, University of Chicago, Drexel University, Fermilab, the Institute for Advanced Study, the Japan Participation Group, Johns Hopkins University, the Joint Institute for Nuclear Astrophysics, the Kavli Institute for Particle Astrophysics and Cosmology, the Korean Scientist Group, the Chinese Academy of Sciences (LAMOST), Los Alamos National Laboratory, the Max Planck Institute for Astronomy (MPIA), the Max Planck Institute for Astrophysics (MPA), New Mexico State University, Ohio State University, University of Pittsburgh, University of Portsmouth, Princeton University, the United States Naval Observatory, and the University of Washington.

ORCID iDs

Tania M. Barone https://orcid.org/0000-0002-2784-564X
Francesco D'Eugenio https://orcid.org/0000-0003-2388-8172
Matthew Colless https://orcid.org/0000-0001-9552-8075
Nicholas Scott https://orcid.org/0000-0001-8495-8547

References

Abazajian, K. N., Adelman-McCarthy, J. K., Agüeros, M. A., et al. 2009, ApJS, 182, 543
Amorisco, N. C. 2017, MNRAS, 464, 2882
Baldwin, J. A., Phillips, M. M., & Terlevich, R. 1981, PASP, 93, 5
Barone, T. M., D'Eugenio, F., Colless, M., et al. 2018, ApJ, 856, 64
Barro, G., Faber, S. M., Pérez-González, P. G., et al. 2013, ApJ, 765, 104
Bell, E. F. 2008, ApJ, 682, 355
Bell, E. F., van der Wel, A., Papovich, C., et al. 2012, ApJ, 753, 167
Bernardi, M., Sheth, R. K., Nichol, R. C., Schneider, D. P., & Brinkmann, J. 2005, AJ, 129, 61
Bluck, A. F. L., Mendel, J. T., Ellison, S. L., et al. 2014, MNRAS, 441, 599
Boecker, A., Leaman, R., van de Ven, G., et al. 2020, MNRAS, 491, 823
Boylan-Kolchin, M., & Ma, C.-P. 2007, MNRAS, 374, 1227
Brinchmann, J., Charlot, S., White, S. D. M., et al. 2004, MNRAS, 351, 1151
Bruzual, G., & Charlot, S. 2003, MNRAS, 344, 1000
Bryant, J. J., Owers, M. S., Robotham, A. S. G., et al. 2015, MNRAS, 447, 2857
Bundy, K., Bershady, M. A., Law, D. R., et al. 2015, ApJ, 798, 7
Cappellari, M. 2017, MNRAS, 466, 798
Cappellari, M., & Emsellem, E. 2004, PASP, 116, 138
Cappellari, M., Emsellem, E., Krajnović, D., et al. 2011, MNRAS, 413, 813
Cappellari, M., McDermid, R. M., Alatalo, K., et al. 2012, Natur, 484, 485
Cappellari, M., McDermid, R. M., Alatalo, K., et al. 2013, MNRAS, 432, 1862
Cappellari, M., Verolme, E. K., van der Marel, R. P., et al. 2002, ApJ, 578, 787
Chabrier, G. 2003, PASP, 115, 763
Chang, Y.-Y., van der Wel, A., da Cunha, E., & Rix, H.-W. 2015, ApJS, 219, 8
Chauke, P., van der Wel, A., Pacifici, C., et al. 2019, ApJ, 877, 48
Cheung, E., Faber, S. M., Koo, D. C., et al. 2012, ApJ, 760, 131
Cimatti, A., Cassata, P., Pozzetti, L., et al. 2008, A&A, 482, 21
Cleveland, W. S., & Devlin, S. J. 1988, J. Am. Stat. Assoc., 83, 596
Conroy, C., & van Dokkum, P. G. 2012, ApJ, 760, 71
Cook, B. A., Conroy, C., Pillepich, A., Rodriguez-Gomez, V., & Hernquist, L. 2016, ApJ, 833, 158
Croom, S. M., Lawrence, J. S., Bland-Hawthorn, J., et al. 2012, MNRAS, 421, 872
D'Eugenio, F., Colless, M., Groves, B., Bian, F., & Barone, T. M. 2018, MNRAS, 479, 1807
Di Matteo, P., Pipino, A., Lehnert, M. D., Combes, F., & Semelin, B. 2009, A&A, 499, 427
Díaz-García, L. A., Cenarro, A. J., López-Sanjuan, C., et al. 2019, A&A, 631, A158
Eldridge, J. J., Stanway, E. R., Xiao, L., et al. 2017, PASA, 34, e058
Faber, S. M. 1973, ApJ, 179, 731
Falcón-Barroso, J., Sánchez-Blázquez, P., Vazdekis, A., et al. 2011, A&A, 532, A95
Ferreras, I., Scott, N., Barbera, F. L., et al. 2019, MNRAS, 489, 608
Foreman-Mackey, D., Hogg, D. W., Lang, D., & Goodman, J. 2013, PASP, 125, 306
Franx, M., van Dokkum, P. G., Förster Schreiber, N. M., et al. 2008, ApJ, 688, 770
Gallazzi, A., Charlot, S., Brinchmann, J., & White, S. D. M. 2006, MNRAS, 370, 1106
Gallazzi, A., Charlot, S., Brinchmann, J., White, S. D. M., & Tremonti, C. A. 2005, MNRAS, 362, 41
Ganda, K., Peletier, R. F., McDermid, R. M., et al. 2007, MNRAS, 380, 506
García-Burillo, S., Combes, F., Usero, A., et al. 2014, A&A, 567, A125
Goddard, D., Thomas, D., Maraston, C., et al. 2017, MNRAS, 465, 688
González Delgado, R. M., García-Benito, R., Pérez, E., et al. 2015, A&A, 581, A103

Goodman, J., & Weare, J. 2010, Communications in Applied Mathematics and Computational Science, 5, 65
Greene, J. E., Veale, M., Ma, C.-P., et al. 2019, ApJ, 874, 66
Greggio, L., & Renzini, A. 1983, A&A, 118, 217
Hirschmann, M., Naab, T., Ostriker, J. P., et al. 2015, MNRAS, 449, 528
Hunter, J. D. 2007, CSE, 9, 90
Jones, E., Oliphant, T., Peterson, P., et al. 2001, SciPy: Open Source Scientific Tools for Python, http://www.scipy.org/
Kauffmann, G., Heckman, T. M., Tremonti, C., et al. 2003a, MNRAS, 346, 1055
Kauffmann, G., Heckman, T. M., White, S. D. M., et al. 2003b, MNRAS, 341, 54
Kauffmann, G., White, S. D. M., Heckman, T. M., et al. 2004, MNRAS, 353, 713
Kennicutt, R. C., & Evans, N. J. 2012, ARA&A, 50, 531
Kennicutt, R. C., Jr. 1998, ApJ, 498, 541
Kewley, L. J., Dopita, M. A., Sutherland, R. S., Heisler, C. A., & Trevena, J. 2001, ApJ, 556, 121
Kobayashi, C. 2004, MNRAS, 347, 740
Kriek, M., van Dokkum, P. G., Franx, M., Illingworth, G. D., & Magee, D. K. 2009, ApJL, 705, L71
Kroupa, P. 2001, MNRAS, 322, 231
La Barbera, F., Ferreras, I., Vazdekis, A., et al. 2013, MNRAS, 433, 3017
Lang, P., Wuyts, S., Somerville, R. S., et al. 2014, ApJ, 788, 11
Li, H., Ge, J., Mao, S., et al. 2017, ApJ, 838, 77
Li, H., Mao, S., Cappellari, M., et al. 2018, MNRAS, 476, 1765
Lian, J., Thomas, D., Maraston, C., et al. 2018, MNRAS, 474, 1143
Lilly, S. J., & Carollo, C. M. 2016, ApJ, 833, 1
Liu, Y., Peng, E. W., Blakeslee, J., et al. 2016, ApJ, 818, 179
Madau, P., & Dickinson, M. 2014, ARA&A, 52, 415
Marks, M., Kroupa, P., Dabringhausen, J., & Pawlowski, M. S. 2012, MNRAS, 422, 2246
Martín-Navarro, I., Brodie, J. P., van den Bosch, R. C. E., Romanowsky, A. J., & Forbes, D. A. 2016, ApJL, 832, L11
Martín-Navarro, I., La Barbera, F., Vazdekis, A., Falcón-Barroso, J., & Ferreras, I. 2015a, MNRAS, 447, 1033
Martín-Navarro, I., Lyubenova, M., van de Ven, G., et al. 2019, A&A, 626, A124
Martín-Navarro, I., Vazdekis, A., Falcón-Barroso, J., et al. 2018, MNRAS, 475, 3700
Martín-Navarro, I., Vazdekis, A., La Barbera, F., et al. 2015b, ApJL, 806, L31
Matteucci, F. 1994, A&A, 288, 57
Matteucci, F. 2012, Chemical Evolution of Galaxies (Berlin: Springer-Verlag)
McDermid, R. M., Alatalo, K., Blitz, L., et al. 2015, MNRAS, 448, 3484
Møller, P., & Christensen, L. 2020, MNRAS, 492, 4805
Nelan, J. E., Smith, R. J., Hudson, M. J., et al. 2005, ApJ, 632, 137
Norris, M. A., Escudero, C. G., Faifer, F. R., et al. 2015, MNRAS, 451, 3615
Omand, C. M. B., Balogh, M. L., & Poggianti, B. M. 2014, MNRAS, 440, 843
Oser, L., Ostriker, J. P., Naab, T., Johansson, P. H., & Burkert, A. 2010, ApJ, 725, 2312
Pagel, B. E. J., & Tautvaisiene, G. 1995, MNRAS, 276, 505
Parikh, T., Thomas, D., Maraston, C., et al. 2018, MNRAS, 477, 3954
Peletier, R. F., Falcón-Barroso, J., Bacon, R., et al. 2007, MNRAS, 379, 445
Perez, F., & Granger, B. E. 2007, CSE, 9, 21
Pietrinferni, A., Cassisi, S., Salaris, M., & Castelli, F. 2004, ApJ, 612, 168
Pietrinferni, A., Cassisi, S., Salaris, M., & Castelli, F. 2006, ApJ, 642, 797
Pillepich, A., Vogelsberger, M., Deason, A., et al. 2014, MNRAS, 444, 237
Pipino, A., D'Ercole, A., Chiappini, C., & Matteucci, F. 2010, MNRAS, 407, 1347
Pointon, S. K., Kacprzak, G. G., Nielsen, N. M., et al. 2019, ApJ, 883, 78
Press, W. H., Flannery, B. P., Teukolsky, S. A., Vetterling, W. T., & Gould, H. 1987, AmJPh, 55, 90
Press, W. H., Teukolsky, S. A., Vetterling, W. T., & Flannery, B. P. 1992, Numerical Recipes in FORTRAN (2nd ed.): The Art of Scientific Computing (Cambridge: Cambridge Univ. Press)
Prochaska, J. X., Werk, J. K., Worseck, G., et al. 2017, ApJ, 837, 169
Reichard, T. A., Heckman, T. M., Rudnick, G., et al. 2009, ApJ, 691, 1005
Robaina, A. R., Hoyle, B., Gallazzi, A., et al. 2012, MNRAS, 427, 3006
Astropy Collaboration, Robitaille, T. P., Tollerud, E. J., et al. 2013, A&A, 558, A33
Rodriguez-Gomez, V., Pillepich, A., Sales, L. V., et al. 2016, MNRAS, 458, 2371
Sakamoto, K., Aalto, S., Combes, F., Evans, A., & Peck, A. 2014, ApJ, 797, 90
Salim, S., Rich, R. M., Charlot, S., et al. 2007, ApJS, 173, 267
Salpeter, E. E. 1955, ApJ, 121, 161
Sánchez-Blázquez, P., Gorgas, J., Cardiel, N., & González, J. J. 2006a, A&A, 457, 809
Sánchez-Blázquez, P., Peletier, R. F., Jiménez-Vicente, J., et al. 2006b, MNRAS, 371, 703
Sánchez-Blázquez, P., Rosales-Ortega, F. F., Méndez-Abreu, J., et al. 2014, A&A, 570, A6
Schawinski, K., Kaviraj, S., Khochfar, S., et al. 2007b, ApJS, 173, 512
Schawinski, K., Thomas, D., Sarzi, M., et al. 2007a, MNRAS, 382, 1415
Schiavon, R. P. 2007, ApJS, 171, 146
Schmidt, M. 1959, ApJ, 129, 243
Scott, N., Brough, S., Croom, S. M., et al. 2017, MNRAS, 472, 2833
Scott, N., Cappellari, M., Davies, R. L., et al. 2009, MNRAS, 398, 1835
Scott, N., Cappellari, M., Davies, R. L., et al. 2013, MNRAS, 432, 1894
Scott, N., van de Sande, J., Croom, S. M., et al. 2018, MNRAS, 481, 2299
Serra, P., & Trager, S. C. 2007, MNRAS, 374, 769
Sérsic, J. L. 1968, Atlas de Galaxias Australes (Córdoba, Argentina: Observatorio Astronomico, Universidad Nacional de Cordoba)
Shen, S., Madau, P., Guedes, J., et al. 2013, ApJ, 765, 89
Shen, S., Mo, H. J., White, S. D. M., et al. 2003, MNRAS, 343, 978
Simard, L., Mendel, J. T., Patton, D. R., Ellison, S. L., & McConnachie, A. W. 2011, ApJS, 196, 11
Spiniello, C., Trager, S., Koopmans, L. V. E., & Conroy, C. 2014, MNRAS, 438, 1483
Stanway, E. R., & Eldridge, J. J. 2018, MNRAS, 479, 75
Storn, R., & Price, K. 1997, Journal of Global Optimization, 11, 341
Strauss, M. A., Weinberg, D. H., Lupton, R. H., et al. 2002, AJ, 124, 1810
Szomoru, D., Franx, M., & van Dokkum, P. G. 2012, ApJ, 749, 121
Tacconi, L. J., Neri, R., Genzel, R., et al. 2013, ApJ, 768, 74
Taylor, M. B. 2005, in ASP Conf. Ser. 347, Astronomical Data Analysis Software and Systems XIV, ed. P. Shopbell, M. Britton, & R. Ebert (San Francisco, CA: ASP), 29
Thomas, D., Greggio, L., & Bender, R. 1998, MNRAS, 296, 119
Thomas, D., Maraston, C., Bender, R., & Mendes de Oliveira, C. 2005, ApJ, 621, 673
Thomas, D., Maraston, C., & Johansson, J. 2011, MNRAS, 412, 2183
Thomas, D., Maraston, C., Schawinski, K., Sarzi, M., & Silk, J. 2010, MNRAS, 404, 1775
Thomas, D., Steele, O., Maraston, C., et al. 2013, MNRAS, 431, 1383
Trager, S. C., Faber, S. M., Worthey, G., & González, J. J. 2000, AJ, 120, 165
Trager, S. C., & Somerville, R. S. 2009, MNRAS, 395, 608
Trujillo, I., Conselice, C. J., Bundy, K., et al. 2007, MNRAS, 382, 109
van de Sande, J., Scott, N., Bland-Hawthorn, J., et al. 2018, NatAs, 2, 483
van der Walt, S., Colbert, S. C., & Varoquaux, G. 2011, CSE, 13, 22
van der Wel, A., Franx, M., van Dokkum, P. G., et al. 2014, ApJ, 788, 28
van der Wel, A., Holden, B. P., Zirm, A. W., et al. 2008, ApJ, 688, 48
van Dokkum, P., Conroy, C., Villaume, A., Brodie, J., & Romanowsky, A. J. 2017, ApJ, 841, 68
van Dokkum, P. G., Brammer, G., Fumagalli, M., et al. 2011, ApJL, 743, L15
van Dokkum, P. G., & Conroy, C. 2010, Natur, 468, 940
van Dokkum, P. G., Franx, M., Kriek, M., et al. 2008, ApJL, 677, L5
Vaughan, S. P., Davies, R. L., Zieleniewski, S., & Houghton, R. C. W. 2018, MNRAS, 479, 2443
Vazdekis, A., Coelho, P., Cassisi, S., et al. 2015, MNRAS, 449, 1177
Vazdekis, A., Sánchez-Blázquez, P., Falcón-Barroso, J., et al. 2010, MNRAS, 404, 1639
Veilleux, S., & Osterbrock, D. E. 1987, ApJS, 63, 295
Vincenzo, F., Matteucci, F., Belfiore, F., & Maiolino, R. 2016, MNRAS, 455, 4183
Wake, D. A., van Dokkum, P. G., & Franx, M. 2012, ApJL, 751, L44
Wellons, S., Torrey, P., Ma, C.-P., et al. 2015, MNRAS, 449, 361
Wellons, S., Torrey, P., Ma, C.-P., et al. 2016, MNRAS, 456, 1030
Whitaker, K. E., Bezanson, R., van Dokkum, P. G., et al. 2017, ApJ, 838, 19
Williams, R. J., Quadri, R. F., Franx, M., et al. 2010, ApJ, 713, 738
Woo, J., Carollo, C. M., Faber, S. M., Dekel, A., & Tacchella, S. 2017, MNRAS, 464, 1077
Woo, J., Dekel, A., Faber, S. M., & Koo, D. C. 2015, MNRAS, 448, 237
Woo, J., & Ellison, S. L. 2019, MNRAS, 487, 1927
Worthey, G. 1992, PhD thesis, Univ. California, Santa Cruz
Wright, E. L., Eisenhardt, P. R. M., Mainzer, A. K., et al. 2010, AJ, 140, 1868
Wuyts, S., Förster Schreiber, N. M., van der Wel, A., et al. 2011, ApJ, 742, 96
York, D. G., Adelman, J., Anderson, J. E., Jr., et al. 2000, AJ, 120, 1579